Investigation of underground cavities in a two-layer model using the refraction seismic method

Tihomir Engelsfeld[1*], Franjo Šumanovac[2] and Nenad Pavin[3†]

[1] *Department of Geophysics, Faculty of Science, University of Zagreb, Zagreb, Croatia*
[2] *Faculty of Mining, Geology and Petroleum Engineering, University of Zagreb, Pierottijeva 6, 10000 Zagreb, Croatia*
[3] *Department of Physics, Faculty of Science, University of Zagreb, Zagreb, Croatia*

ABSTRACT

This paper presents a new approach to the investigation of underground cavities. Our technique is based on the refraction seismic method. We have studied a two-dimensional, two-layer geological model. In our model, the lower seismic velocity layer is situated above the higher seismic velocity layer, with a circular cavity positioned within the upper layer. We have investigated the influence exerted by the cavity on the first arrivals of seismic waves. The obtained traveltimes are solutions of the eikonal equation and are presented using the time-distance graph. All refracted waves encountering the cavity have to circumvent it, as it represents an impediment to the propagation of seismic energy. This circumvention causes delays in the first arrivals of the seismic waves at the surface as compared to traveltimes with no cavity present. These delays create a characteristic shape of the time-distance graph, characterized by the peak point in which the plot line has a discontinuous change. Using this graph and analysing the delays of the first arrivals, we have derived expressions for determining both the position and size of the circular cavity. The practical application of the derived relations has been tested on a model test site built in a natural rock setting. This simple method indicates the presence of the cavity. The accuracy of the calculated cavity parameters: the horizontal position x, the depth z and cavity radius r depends on the geophone spacing. For geophone spacing equal to or less than the cavity radius, the accuracy of the method is shown to be acceptable. The maximal estimated error is equal to a half geophone spacing. Finally, we have demonstrated that this method is also applicable in the detection of non-circular cavities.

INTRODUCTION

One of the most serious civil engineering problems found at construction sites is the occurrence of underground cavities. The threat of undetected cavity collapse can be catastrophic, requiring a precise positioning of these cavities prior to the construction of dams, roads, tunnels, etc. (Musset and Khan 2000). Encountered cavities can be man-made, such as abandoned coal mines or natural, which are particularly frequent in karst regions. Cavities may vary greatly, not only in size and shape but also in their burial depth.

During the past decade, different techniques (based on various geophysical methods) have been developed for adequate cavity detection. Seismic methods are mostly based on the analysis of P-wave reflection (Grandjean *et al.* 2002) and surface-wave diffraction (Leparoux *et al.* 2000). Grandjean and Leparoux (2004) investigated the potential of several seismic methods for detecting cavities and buried objects. They focused their atten-

tion on the interaction between different types of seismic waves and the cavity itself. This interaction may also be studied using numerical modelling as well as experimentally at test sites built specifically for that purpose. However, as the dimensions of these test sites are substantially smaller than those of real geological structures, special attention needs to be devoted when applying these methods to real geological conditions (Grandjean and Leparoux 2004). Seismic behaviour depends on various factors, particularly on the nature of the seismic wave and on the ratio between the wavelength and cavity size. Depending on these factors, it has been shown that a cavity can act as a diffraction body (Baker *et al.* 1997) and that the phase velocity and attenuation characteristics of surface waves can be used to detect near-surface anomalies of various kinds (Park *et al.* 1998). Several research groups have studied practical applications of seismic methods for cavity and buried objects detection. Piwakowski *et al.* (1997a,b) and Gochioco (1990) applied the reflection seismic method for detecting old gypsum and coal mines. Herman *et al.* (2000) showed that Rayleigh waves are suitable for shallow object imaging. Grandjean (2006) studied subsurface object imaging by seismic P-wave tomography. Other

---

* tihomir.engelsfeld@phy.hr

† Now at: Max Planck Institute for the Physics of Complex Systems, Dresden 01187, Germany

researchers have mainly focused on theoretical aspects of the problem. Gelis *et al.* (2005) studied the interaction of seismic surface waves with shallow cavities using numerical modelling. Ganji *et al.* (1997) developed methods for detecting underground obstacles based on spectral analysis of surface waves (SASW).

In this paper, we have investigated the application of the seismic refraction method in researching underground cavities in a two-layer model. We have studied the influence of the cavity on the first arrivals of seismic waves. The traveltimes (presented in the time-distance ($t - x$) graph) were calculated by solving the eikonal equation. Application of the eikonal equation for the calculation of traveltimes began in the late 1980s and since then, different approaches have been proposed for 2D (Vidale 1988; Podvin and Lecomte 1991; Qin *et al.* 1992; Cao and Greenhalgh 1994) and 3D cases (Vidale 1990; Sethian and Popovici 1999; Vanelle and Gajewski 2002). These methods are based on algorithms implemented in Cartesian coordinates. Sun and Fomel (1998) implemented an eikonal solver in the trigonal 2D and the tetragonal 3D coordinates, while Alkhalifah and Fomel (2001) showed the advantages of using spherical coordinates. In addition to traveltime calculation Buske and Kästner (2004) developed the method that also calculates the amplitudes of the first arrivals. A comparative review of the different methods is given by Leidenfrost *et al.* (1999) and Kim (2002).

In the first step, we have used Huygen's principle to explain the circumvention of refracted waves around the cavity. The consequence of this circumvention is a delay of the first arrivals of seismic waves at the surface. Through the use of these delays, we have explained the shape of the $t - x$ graph and we have derived equations that determine the position and the size of the circular cavity in a two-layer model. We have also shown the applicability of the method in the case of non-circular cavities. Our technique has been developed for models with a flat surface topography. Using static corrections, the influence of land surface topography variations on first arrivals can be eliminated (Musset and Khan 2000).

Finally, we have applied our method to experimental data. A test site built in a natural environment allowed us to investigate both the advantages and limitations of the developed method in real field conditions. A dry sand layer above a wet sand layer simulates a two-layer model, where the interface between the layers is defined by the level of the underground water. We have discussed the influence of various factors on the accuracy of the obtained cavity parameters (e.g., depth, size, etc.).

EIKONAL EQUATION

In 2D, the eikonal equation has the following form:

$$\left(\frac{\partial t}{\partial x}\right)^2 + \left(\frac{\partial t}{\partial z}\right)^2 = s^2(x, z), \tag{1}$$

where $t = t(x, z)$ represents the traveltime at the point (x, z) and $s(x, z)$ the slowness, which is defined as the reciprocal value of the velocity at point (x, z). The slowness distribution is known for
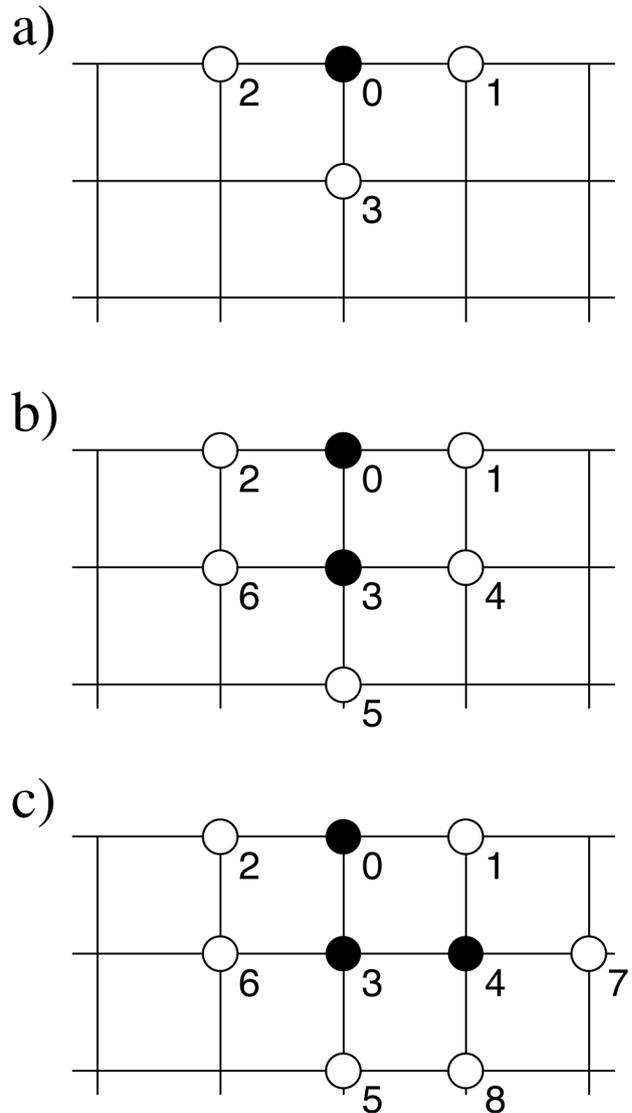

FIGURE 1

The first few steps in the traveltime calculation procedure. Black circles represent fixed points while the white circles represent the instantaneous wavefront. a) The traveltimes are calculated at points 1, 2 and 3 around the source 0. b) The traveltimes are calculated at points 4, 5 and 6 around the fixed point 3. c) The traveltimes are calculated at points 1, 7 and 8 around the fixed point 4.

all points of the 2D grid and the traveltimes are calculated for all grid points. The grid comprises $N \times N$ squares. In general, the basis of the method can be described as a finite-difference calculation of point-to-point traveltimes in the complete 2D grid. It is necessary to choose the appropriate algorithm to ensure that the first arrival condition is fulfilled. The applied algorithm, characterized by high accuracy, is based on the expanding wavefronts method and was first introduced by Qin *et al.* (1992). The complete mathematical theory of this method is given by Sethian (1996).
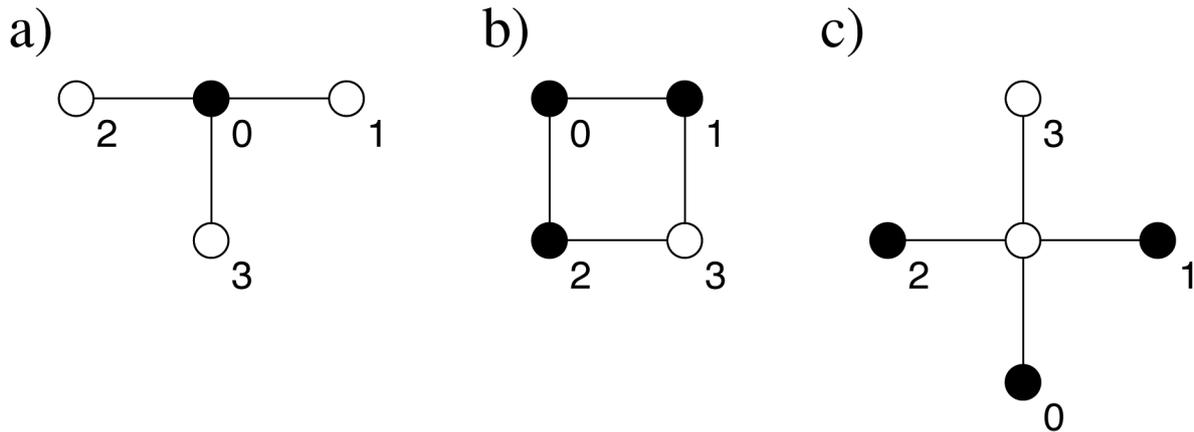
a)

b)

c)

FIGURE 2

Application of the extrapolation formulas. The black circles indicate the points with known traveltimes, while white circles indicate the points for which the traveltimes are being calculated. a) Scheme for extrapolation equation (2). b) Scheme for extrapolation equation (3). c) Scheme for extrapolation equation (4).

The implemented algorithm

The wave source is defined as the initial point with coordinate (0, 0). At this point the traveltime is $t = 0$ and we declare this point fixed. The fixed points are defined as those for which the associated traveltime can no longer be varied. The calculation proceeds by calculating the traveltime at three neighbouring points. These three points form the instantaneous wavefront. The traveltimes at all points of the instantaneous wavefront are then ordered by magnitude and the point with the lowest value is chosen. This point is now declared fixed and the traveltimes of the neighbouring points are computed. The calculation is repeated for all points that are not fixed points, as well as those that have not already been calculated. The values at the points will be updated if the previously calculated value exceeds the presently calculated value. The newly calculated points and the remaining points of the instantaneous wavefront now form the new instantaneous wavefront. The points at this new instantaneous wavefront are again ordered by magnitude and the one with the lowest associated value is chosen as a fixed point. This procedure is repeated until the times at all points of the grid are calculated. The initial few steps in the calculation of the observed expanding wavefront are given in schematic form in Fig. 1.

Three different extrapolation formulas are used to obtain the traveltimes. In the first step, the traveltime at points neighbouring the source of the wave are calculated using the linear extrapolation:

$$t_i = h\frac{s_0 + s_i}{2}, \quad i = 1, 2, 3 \tag{2}$$

where h is the distance between neighbouring points and $(s_0 + s_i)/2$ is the average value of the slowness between source point s_0 and point s_i (Fig. 2a). For all other points, the following formulas are used (Fig. 2b):

$$t_3 = t_0 + \sqrt{2(hs)^2 - (t_2 - t_1)^2} \tag{3}$$

or (Fig. 2c):

$$t_3 = t_0 + \sqrt{4(hs)^2 - (t_2 - t_1)^2} \tag{4}$$

where in the both cases, t_0 is the first arrival at the fixed point, t_1 and t_2 are already calculated traveltimes at the adjacent points and t_3 is the value being calculated. The slowness s is the average value of the slowness at points 0, 1, 2 and 3; $s = (s_0 + s_1 + s_2 + s_3)/4$.

Seismic energy does not propagate through the cavity. The velocity of the seismic wave in the cavity is zero and the slowness tends to infinity. To avoid infinite values in the calculation, the velocity of the wave in the cavity has been defined as 5 m/s. This approximation has a negligible effect on the accuracy, as the slowest seismic velocities are more than 50 times greater.

Although the implemented algorithm is predominantly stable (Qin *et al.* 1992), the occurrence of negative values inside the square root in the extrapolation formulas is also possible. This instability is a consequence of extremely large jumps in seismic velocities at the edge of the cavity. The problem can be avoided through smoothing of the slowness model. We have used a 1D smoothing operator that is described and applied by Leidenfrost *et al.* (1999).

For the $(n+1)^{th}$ iteration the smoothing operator is given by:

$$s^{n+1}(i) = \frac{s^n(i-1)}{4} + \frac{s^n(i)}{2} + \frac{s^n(i+1)}{4}. \tag{5}$$

The 1D smoothing operator is applied five times to both dimensions.

THE INFLUENCE OF THE CAVITY ON THE FIRST ARRIVALS OF SEISMIC WAVES

We investigated a two-layer geological model where the layer with a lower seismic velocity v_1 is above the layer with a higher seismic velocity v_2. The boundary between the layers is parallel to the surface and is at a depth h. The cavity is circular in shape with a radius r and positioned in the top layer with its centre at depth z. The horizontal distance of the centre of the cavity from the left edge of the profile is denoted by x (Fig. 3). The source of the seismic energy is positioned on the left-hand side of the profile.

Numerical modelling

Numerical modelling with the eikonal equation is used to calculate the traveltimes in the entire 2D profile where r = 2 m, z = 3 m, x = 20 m, d = 35 m, h = 6 m, v_1 = 300 m/s and v_2 = 1500 m/s. The dimension of the extrapolation grid is 4000 × 4000. The calculated traveltimes are presented in two ways. Figure 4(a) depicts the traveltimes in the time-distance graph and Fig. 4(b) the propagation of the wavefronts. The time spacing used between two wavefronts is t = 0.0009 s (Fig. 4b). Both presentations help to explain the propagation of seismic waves through the geological model.

Propagation of the refracted waves around the cavity

The influence of the cavity on the $t - x$ graph is visible between the distances x_1 and x_2 (Fig. 4). Outside this area, the graph exhibits the same behaviour as it does without the cavity. The area between x_1 and x_2 consists in two distinct regions. The first, between x_1 and x_p is characterized by a gradual increase in the slope, while the second, between x_p and x_2 is characterized by a gradual decrease. The point at which the slope of the graph changes discontinuously is designated x_p and called the peak
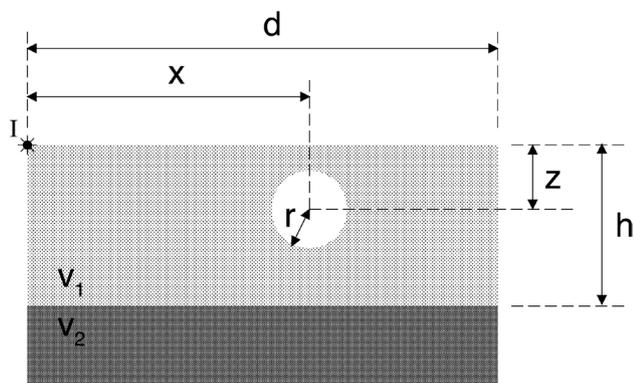
point. Shown in Fig. 4(b), z_1 indicates the last unaffected ray of the refracted wave before the influence of the cavity becomes visible, while z_2 indicates the first unaffected ray after the cavity influence has ceased. The rays z_1 and z_2 exit the surface at distances x_1 and x_2 respectively.

To be able to explain a typical shape of the $t - x$ graph, we investigated the behaviour of the seismic waves in the cavity region. The cavity represents a barrier to the propagation of the seismic waves and therefore, the refracted waves have to circumvent it. The circumvention of the seismic energy around the cavity is explained by using Huygen's principle, where each point of the wavefront is the source of a new wave (Fig. 5). The points at the boundary of the cavity are also new source points. As can be seen, the rays belonging to the first arrivals are tangential to the cavity.
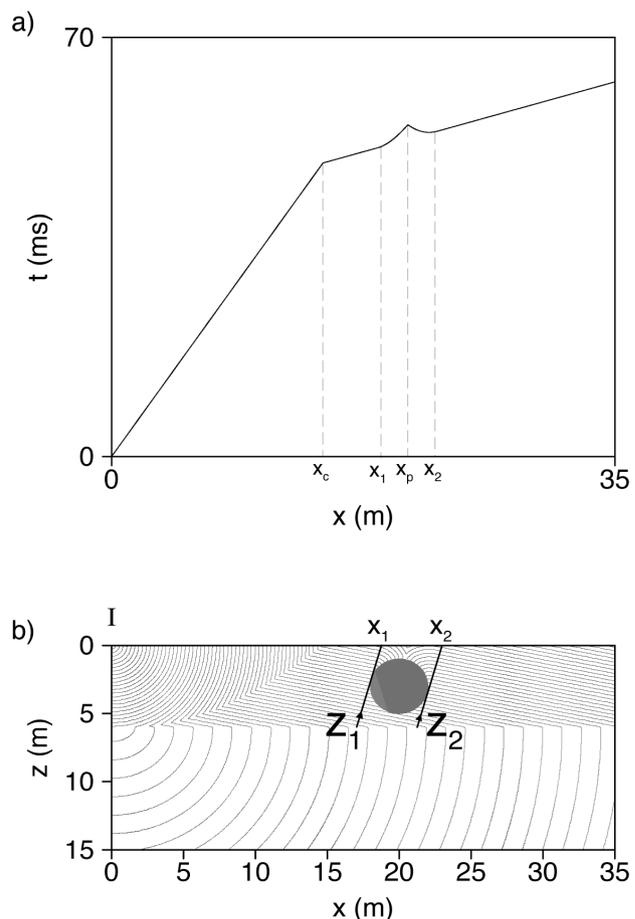
FIGURE 3

A two-layer geological model. A cavity of radius r at a depth z. The velocities of propagation in the top and bottom layer are v_1 and v_2, respectively. The horizontal distance of the centre of the cavity from the source I is denoted by x, the depth of the boundary between the layers by h and the profile length by d.

FIGURE 4

a) The $t - x$ graph for the cavity in a two-layer model. Refracted waves are fastest beyond the crossover distance x_c. The distances at which the influence of the cavity starts (stops) are x_1 (x_2), while x_p is the peak point. b) The spread of the wavefront of the first arrivals. The last unaffected ray of the first arrival before the onset of the influence of the cavity is denoted by z_1 and the first ray of the first arrival after the influence of the cavity ceases is denoted by z_2. The rays exit the surface at distance x_1 (for z_1) and x_2 (for z_2).
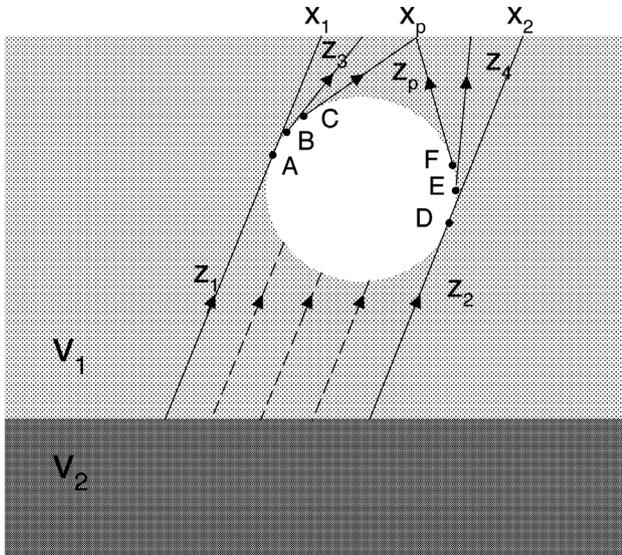
FIGURE 5

The propagation of seismic waves around the cavity. The boundary rays z_1 and z_2 are tangential to the cavity at points A and D. Other capital letters represent new source points. The rays associated with those points are tangential to the edge of the cavity. Both rays z_p arrive at the surface simultaneously. The dashed lines indicate the rays of the refracted waves that cannot form a part of the first arrival.

For the circumvention of the cavity from the left, the source points at the edge of the cavity are placed between points A and C (for example, the source point B and the ray z_3). The fact that the wave goes around the cavity from the left-hand side results in a longer first arrival time than if there was no cavity. On the $t – x$ graph, this is evident through the continuously increasing slope of the graph between points x_1 and x_p.

In the region between x_p and x_2, a decrease in the slope is evident. It results from a decrease in the traveltimes with the increasing distance from the source. Past distance x_p, the first arrivals result from the circumvention of the cavity from the right-hand side. In this case, the source points at the edge of the cavity are placed between points D and F (for example, the source point E and the ray z_4). The ray from point E (including the path from D to E) has a longer distance to traverse in comparison to the ray from point D.

The peak point represents the distance at which waves that circumvent the cavity from the left and the right-hand sides arrive at the same time. The waves that emanate from points C and F arrive at the surface simultaneously. Both waves are represented by rays designated z_p and exit the surface at distance x_p (Fig. 5).

The horizontal distance of the peak point is given by the relation:

$$x_p = \frac{x_1 + x_2}{2} \tag{6}$$

and the traveltime at the peak point by relation:

$$t_p = \frac{1}{v_1}\left[\frac{h}{\cos\theta} + x_p \sin\theta - 2h\sin\theta\tan\theta + \frac{h-z}{\cos\theta} + \right.$$
$$\left. r\left(\frac{\pi}{2} - \arccos\frac{r\cos\theta}{z}\right) + \sqrt{\frac{z^2}{\cos^2\theta} - r^2} \right]. \tag{7}$$

The derivation of the formulas for the horizontal distance of the peak point and for the traveltime at the peak point is presented in the Appendix.

An alternate picture can be obtained using the delay time Δt. The delay time is the difference between the traveltime at the peak point (t_p) and the traveltime at the same distance in the case with no cavity present (t_1):

$$\Delta t = t_p - t_1. \tag{8}$$

The value of t_1 is obtained using the well-known equation:

$$t_1 = \frac{x_p}{v_2} + \frac{2h\cos\theta}{v_1}. \tag{9}$$

The delay time can thus be calculated as:

$$\Delta t = \frac{1}{v_1}\left[-\frac{z}{\cos\theta} + r\left(\frac{\pi}{2} - \arccos\frac{r\cos\theta}{z}\right) + \sqrt{\frac{z^2}{\cos^2\theta} - r^2} \right] \tag{10}$$

DETERMINATION OF THE PARAMETERS OF THE CAVITY USING ANALYTICALLY DERIVED FORMULAS

The cavity parameters are size and position. The size of the circular cavity is defined through its radius r. The position of the cavity is defined by the horizontal distance of its centre from the source x and the depth of the centre of the cavity z. The values of these parameters are determined from the first arrivals (i.e., by applying the $t – x$ graph). Determination of the seismic velocities and the depth of the boundary between layers are standard procedures in refraction seismic methods and are not described in this paper.

The radius of the cavity

To establish the value of the radius r, the distances x_1 and x_2 need to be determined from the $t – x$ graph. Simple geometry (Fig. 6) shows that:

$$2r = (x_2 - x_1)\cos\theta, \tag{11}$$

where θ is the refraction angle obtained from the relation $\sin\theta = v_1/v_2$.

The position of the cavity

Two measurements are used to determine the positional parameters of the cavity (x and z): one with the source of the
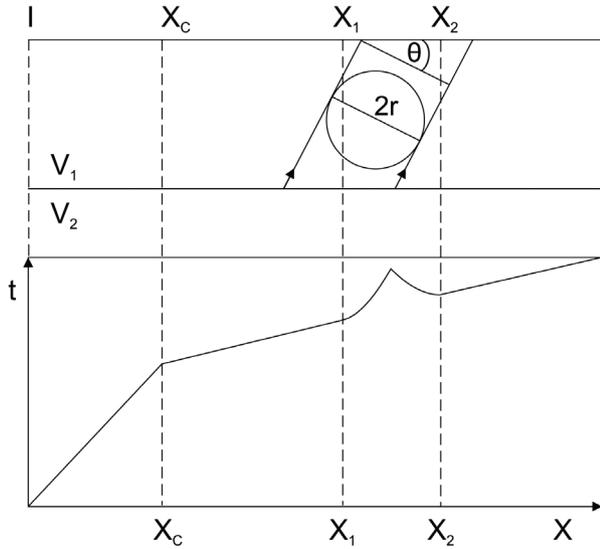
FIGURE 6

The determination of the cavity radius. The diagram shows the correspondence of the boundary rays z_1 and z_2 with the $t - x$ graph. The crossover distance is represented by x_c.
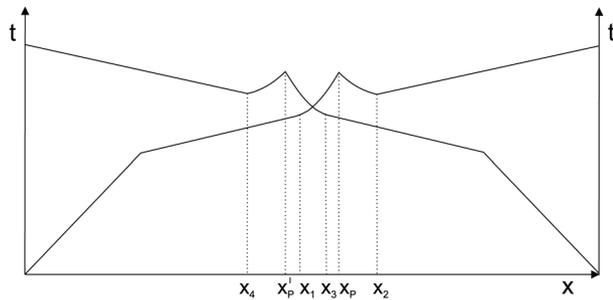

FIGURE 7

The $t - x$ graph for the sources positioned on opposite sides of the seismic profile. The lengths x_1 and x_2 determine the area affected by the cavity for a source to the left, while x_3 and x_4 determine the area affected by the cavity for a source to the right.

wave being to the left side of the cavity and the other to the right. The values x_1, x_2, x_3 and x_4 are obtained from the $t - x$ graph (Fig. 7). All the distances are measured from the position of the left-hand source, i.e., in the positive direction of the x-axis. Figure 8 depicts the last rays of the refracted wave unaffected by the cavity for a source from the left (z_1) and from the right (z_3). It also depicts the first unaffected rays of the refracted wave after the cavity for a source on the left (z_2) and on the right (z_4). The rays z_1, z_2, z_3 and z_4 arrive at the surface at distances x_1, x_2, x_3 and x_4, respectively. Figure 8 shows that depth z can be calculated using the following equations:

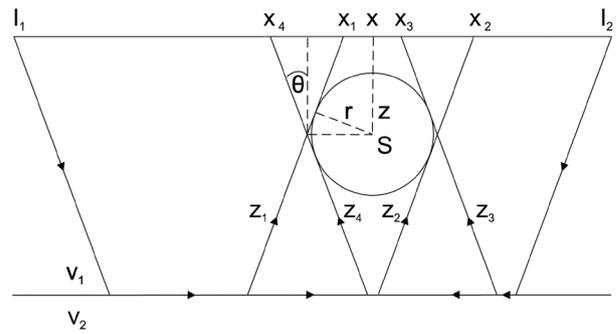$$z = \frac{x_1 - x_4}{2 \tan \theta} \tag{12}$$

FIGURE 8

The determination of the cavity position. The boundary rays z_1 and z_2 (z_3 and z_4) are unaffected by the cavity for a source to the left I_1 (right I_2).

or

$$z = \frac{x_2 - x_3}{2 \tan \theta}. \tag{13}$$

Due to the symmetry of the centre of the cavity with respect to positions x_1 and x_3 or positions x_2 and x_4 (Fig. 8), the horizontal distance x is calculated using the following equations:

$$x = \frac{x_1 + x_3}{2} \tag{14}$$

or

$$x = \frac{x_2 + x_4}{2}. \tag{15}$$

The peak points differ for sources from opposite sides of the cavity (Fig. 7). Applying symmetry, the formula for the position of the peak point for the right-hand source is equivalent to equation (6), which is derived for the left-hand source:

$$x_p' = \frac{x_3 + x_4}{2} \tag{16}$$

The depth can also be determined using either equation (7) or (10). In this instance, the time t_p or delay time Δt have to be read from the $t - x$ graph and the radius r is given by equation (11). Finally, the only unknown variable, depth z, can be calculated using equations (7) or (10), respectively.

Practical experience shows that it is difficult to obtain the precise value of t_p or Δt from the $t - x$ graph. As a result, the more precise way for the determination of the unknown depth z is through the use of equation (12) or (13).

NON-CIRCULAR CAVITY MODELS

We have presented the possibility of using the seismic refraction method in the detection of circular cavities. However, there are various shapes of underground cavities in a natural environment for which the circular assumption is invalid (e.g., tunnels, mine workings, etc.).

Figure 9 shows three shapes of cavities: circular, quadratic and rectangular. The cavities are positioned in the upper layer of a two-layer geological model that is identical to the model described in the previous sections. The boundary rays z_1 and z_2 exit the surface at distances x_1 and x_2. The first arrivals are presented in the $t - x$ graph (Fig. 10). In all cases, a peak point is evident. The existence of a peak point is a strong indication of cavity presence and results from the circumvention of the cavity by the seismic waves and not from the specific shape of the cavity.

Figure 10 also shows that it is almost impossible to distinguish between the graphs for the circular and quadratic cavity because both cavities are in the same position and have similar dimensions (e.g., similar area and circumference). A small difference is visible in the case of the rectangular cavity, which has smaller dimensions than the circular and quadratic cavities. This results in a shorter circumvention and a shorter delay time at the peak point.

The equations that determine the positional parameters are useful not only for circular cavities, as the equations calculate

FIGURE 10

Three $t - x$ graphs for circular (solid line), quadratic (dashed line) and rectangular (dotted line) cavities. The graphs are almost identical. A small difference is visible in the case of the rectangular cavity.

the position of the centre of the cavity. Generally, the size of the cavity is related to the distance between the boundary rays z_1 and z_2 (Figs 9a, 9b and 9c). In the case of the circular cavity, this distance is equal to the diameter of the cavity.

TEST SITE RESEARCH

The aim of this experiment was to examine the applicability of the developed technique in a real environment. An appropriate test site was located at the Trstenik gravel pit situated 10 km east of Zagreb, Croatia. The area consisted of alluvial sedimentary rocks formed through abrasive wear by the river Sava. This location is continuously used for the extraction of gravel and sand. The location, consisting of a layer of dry sand underneath which is a layer of wet sand, was chosen for the testing (Fig. 11a). Preliminary tests (using the standard refraction seismic method) showed that the velocity of the longitudinal waves measured in the dry sand layer was 350 m/s and 1400 m/s in the wet sand layer, resulting in a refraction angle of 14.5°. The boundary between the two layers was at a depth of 2 m. We buried a metal cylindrical tank of 0.5 m radius at a depth of 1.2 m. The central axis of the cylinder was parallel to the surface and perpendicular to the seismic profile (Fig. 11a–c). The tank was filled with air.

The transfer of seismic energy between the dry sand and the metal edge of the tank was negligible, as well as the energy transfer from the metal edge to the air. This is a consequence of the fact that the transmission coefficient is very small between media that have large contrasts in seismic velocity and density (Mussett and Khan 2000).

The 11.5 m long seismic profile was covered by 24 geophones at a spacing of 0.5 m (Fig. 12). The centre of the cavity was directly beneath the 12th geophone; 5.5 m from the left-hand
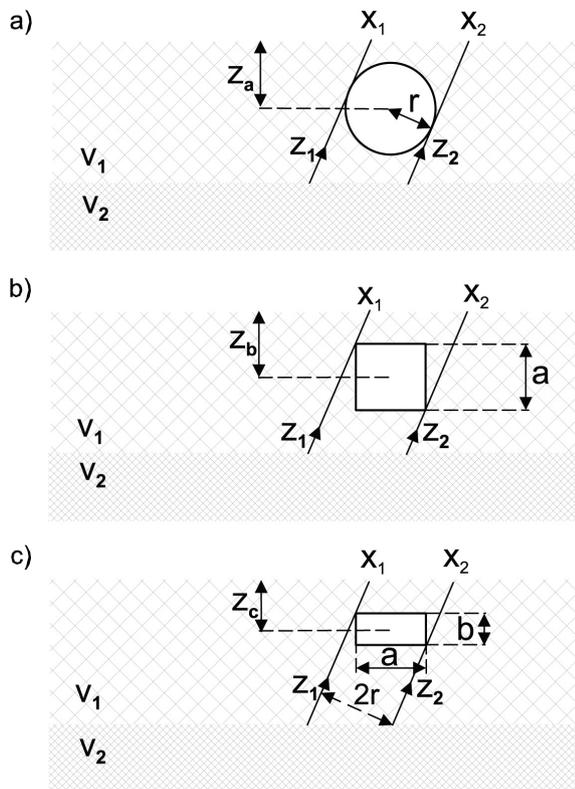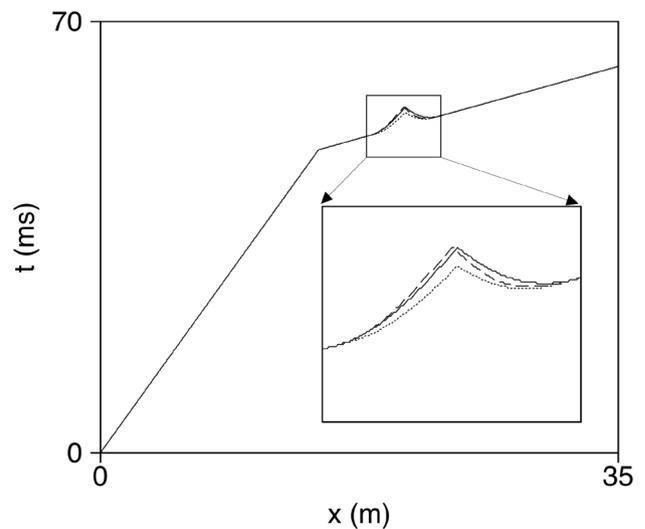

FIGURE 9

Cavities of different shapes in a two-layer model. a) Circular cavity of radius $r = 2$ m at a depth $z_a = 3$ m. b) Quadratic cavity with sides $a = 3.2$ m and the centre of the cavity at a depth $z_b = 3$ m. c) Rectangular cavity with sides $a = 3.2$ m and $b = 1$ m and the centre of the cavity at a depth $z_c = 2.8$ m.
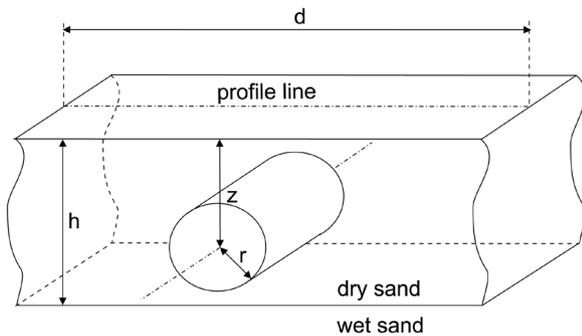
FIGURE 11

a) The location of the test site. The position of a buried tank is indicated by the arrow. b) A cylindrical metal tank was used as a cavity. c) Schematic diagram of the test site. The dry sand layer is situated above a wet sand layer. A cylindrical tank is positioned within the dry sand layer.

end of the seismic profile. We used a 24-channel seismograph with a 120 dB dynamic range. The resonant frequency of the vertical geophones was 100 Hz. The wavelength was $\lambda \approx 3.5$ m, which gives the wavelength-diameter ratio $\lambda/2r \approx 3.5$. The seismic waves were produced through hammer impacts on a metal sheet placed on the surface. We used eight source points. The positions of the sources can be seen in Fig. 12.
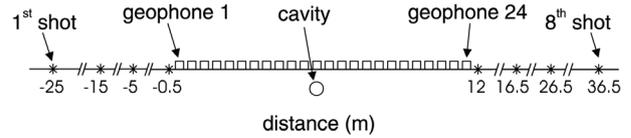

FIGURE 12

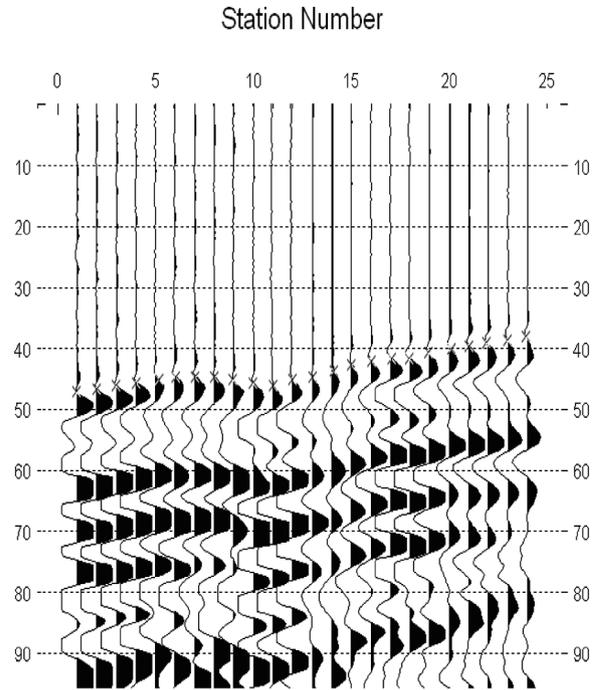Positions of sources and geophones. Sources are represented by stars and geophones by squares.

FIGURE 13

A typical recorded seismogram. The seismogram belongs to the eighth shot. The ordinate axis represents time in milliseconds. The delay of the first arrival at geophone 11 is evident.

Experimental results and data analysis

Figure 13 shows an example of a recorded seismogram that belongs to the 8th shot. The delay of the first arrival at geophone 11 is observable. The recorded traveltimes at all geophones are shown on the $t - x$ graph (Fig. 14). The 4th and 5th shot points are too close to the cavity for their influence to be observed on the graph. In these cases, the shape of the $t - x$ graph is typical of a two-layer model. Some irregularity in the shape of the graphs is a consequence of lateral changes in homogeneities, which led to variations in the seismic velocity. The peak point is visible at the 12th geophone for the 2nd shot and at the 13th geophone for the 1st and 3rd shots. All these sources are positioned to the left of the cavity. For the sources positioned to the right of the cavity, the peak point is visible at the 11th geophone for the 6th, 7th and 8th

TABLE 1

The experimental values of x_1, x_2, x_3 and x_4 as determined from Fig. 14. For all shots, the radius has the same value $r = 0.5$ m. The position of the cavity ($x = 5.4$ m, $z = 1.5$ m) is determined by using average distances (x_1, x_3), and (x_2, x_4), where the influence of the cavity starts and stops, respectively. The maximal estimated error for parameters r, x and z is 0.25 m.

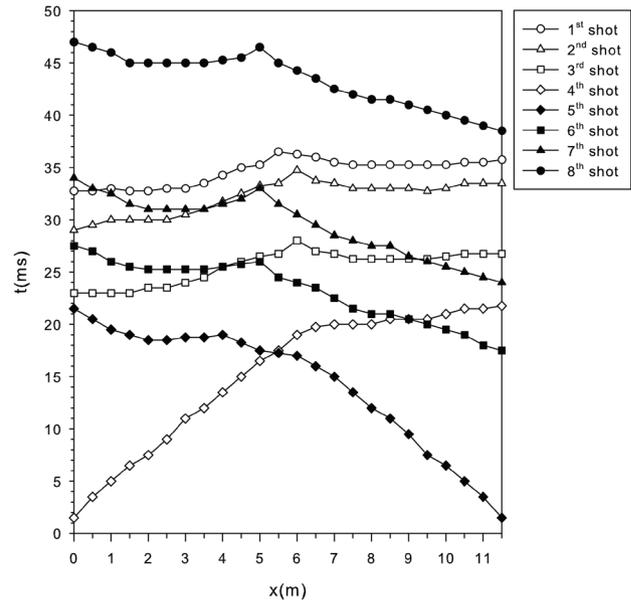| Shot	x^1 (m)	x^2 (m)	x^3 (m)	x^4 (m)
1	5	6	–	–
2	5.5	6.5	–	–
3	5.5	6.5	–	–
4	–	–	–	–
5	–	–	–	–
6	–	–	5.5	4.5
7	–	–	5.5	4.5
8	–	–	5.5	4.5
Average	5.3	6.3	5.5	4.5

FIGURE 14

The $t - x$ graph for the test site measurements. The profile is covered with 24 geophones at a spacing of 0.5 m. The first geophone is positioned at a distance $x = 0$. The peak points are observable at the 12th geophone ($x = 5.5$ m) for the 2nd shot and at the 13th geophone ($x = 6$ m) for the 1st and 3rd shots (for the sources positioned to the left of the cavity). The peak points are observable at the 11th geophone ($x = 5$ m) for the 6th, 7th and 8th shots (for the sources positioned to the right of the cavity). The 4th and 5th shots are too close to the cavity and the influence of the cavity is not visible.

shots. The shape of these six graphs indicates the presence of an underground cavity. The values of x_1, x_2, x_3 and x_4, which determine the area of the cavity's influence, are given in Table 1.

The radius of the cavity

Applying equation (11), the cavity radius for all six shots is calculated independently. In this equation, the difference $x_2 - x_1$ is replaced with the difference $x_3 - x_4$ in the case of the sources to the right of the cavity. This is a consequence of the symmetry depicted in Fig. 8. In all six cases, the calculated cavity radius $r \approx 0.5$ m is in agreement with the radius of the buried cylinder (0.5 m).

The position of the cavity

The depth was obtained using equation (12) or (13) and the horizontal distance is obtained using equation (14) or (15). At least two sources positioned on opposite sides of the cavity are necessary to calculate the horizontal distance, x and the depth, z. We have used the average values of x_1, x_2, x_3 and x_4 in equations (12), (13), (14) and (15). The obtained averages are also given in Table 1. The calculated values of the parameters are: $x = 5.4$ m and $z = 1.5$ m. These results are also in good agreement with the real parameters ($x = 5.5$ m and $z = 1.2$ m). The difference between the real and calculated values in the case of the horizontal distance is 0.1 m (error $\approx 2\%$) and ~0.3 m in case of the depth (error $\approx 15\%$).

The delay time at the peak point

The delay time read from the graphs (Fig. 14) is $\Delta t = (0.8 \pm 0.5)$ ms, where the estimated error of 0.5 ms is influenced by the noise as well as the resolution of the experimental data. A theoretical delay time for our model is 0.3 ms. The experimentally obtained traveltimes are larger than the theoretically calculated traveltimes. This

is because of a loss of homogeneity and decreased sand density in the vicinity of the cavity, resulting from the tank burying process. The velocity of the seismic waves in the disrupted sand near the cavity is lower than 350 m/s. This in turn causes a prolonged delay time for the wave circumventing the cavity.

CONCLUSIONS

The refraction seismic method is a powerful tool for detecting underground cavities. A typical shape of the $t - x$ graph and the occurrence of the peak point strongly indicate the presence of the cavity. Our technique also gives useful formulas for determining the size and position of a circular cavity, which could also be helpful for various non-circular cavity shapes. The practical application of this method was checked in a natural geological environment. In our experiment, a dry sand layer above the wet sand layer simulates a two-layer model. The interface between layers is defined by the ground water. The circular cavity is positioned in the upper layer. The experimentally obtained $t - x$ graph has a visible peak point that indicates the presence of the cavity. Using data from this graph, we calculated the cavity parameters. The results are in good agreement with the real values.

These results underlined both the diffculties that arise in experimental conditions as well as the modes for overcoming the

observed problems. One of the observed problems is the spacing of the geophones in relation to the cavity size. The influence of the cavity on the $t – x$ graph is visible only if a sufficient number of geophones cover the region that yields a typical shape of the graph. A smaller spacing of the geophones yields more accurate results. However, a geophone spacing that is very small will result in no distinguishable difference in traveltimes between neighbouring geophones. It depends on the minimum time interval that the instrument used can distinguish. In our case, the spacing of the geophones is equal to the radius of cavity. This yields acceptable results. Finally, our approach provides the possibility for developing our technique to analyse more complex geological models that could be the subject of future studies. Some of the future investigations will be concentrated on models with dipping or undulating interfaces between layers and on a non-homogeneous velocity model. This will be complemented with the studied refraction method in conjunction with other available methods. This is an important issue, as some existing geological structures perhaps yield $t – x$ graphs similar to the ones observed in the presence of an underground cavity. A decrease in the number of possible interpretations is a continuous goal of research in the field of geophysics.

ACKNOWLEDGEMENTS

APPENDIX

The position of the peak point

We begin to observe the raypaths from point M (Fig. 15). Until reaching position M, the paths of the rays are the same. The circumvention time from the left is given as a sum of $t_{ME} + t_{EA} + t_{AC} + t_{CP}$ and from the right as a sum of $t_{MN} + t_{NB} + t_{BD} + t_{DP}$. These times are equal. In general, t_{XY} designates the traveltime from point X to point Y. Taking into account the relation $t_{ME} = t_{NB}$, it follows that:

$$t_{EA} + t_{AC} + t_{CP} = t_{MN} + t_{BD} + t_{DP}. \tag{A1}$$

The distance from point E to point A is designated as l and from M to N as c_1. It is evident that $t_{EA} = l/v_1$ and $t_{MN} = c_1/v_2$. As $l/c_1 = \sin\theta$, and $v_1/v_2 = \sin\theta$, the times t_{EA} and t_{MN} are equal. Thus, equation (A1) can be reduced to:

$$t_{AC} + t_{CP} = t_{BD} + t_{DP}. \tag{A2}$$

With this we have derived that the traveltimes of the waves circumventing the cavity are the same. The times used in equation (A2) refer to the propagation of the wave within the same medium. Therefore, it is sufficient to observe the length of the rays. Due to mirror symmetry, in terms of the SP-axis, the side AC is equal to BD, as is the length CP to DP. From the above geometric consideration, the peak point is defined by:

$$x_p = \frac{x_1 + x_2}{2}. \tag{A3}$$

The traveltime at the peak point

To find the traveltime at the peak point, the length of the ray that circumvents the cavity is divided into line segments (Fig. 16).
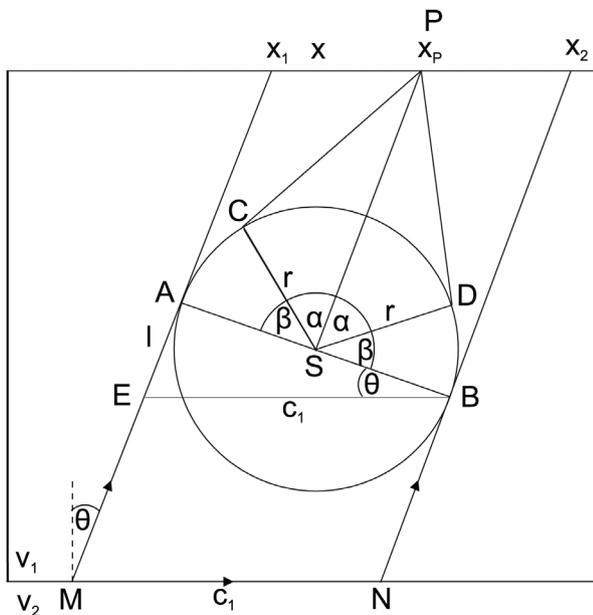

FIGURE 15
The simultaneous arrivals of the waves at the peak point P. The circumvention of the cavity from the left is determined by ray tracing through points M-E-A-C-P while circumvention from the right is determined by ray tracing through points M-N-B-D-P.
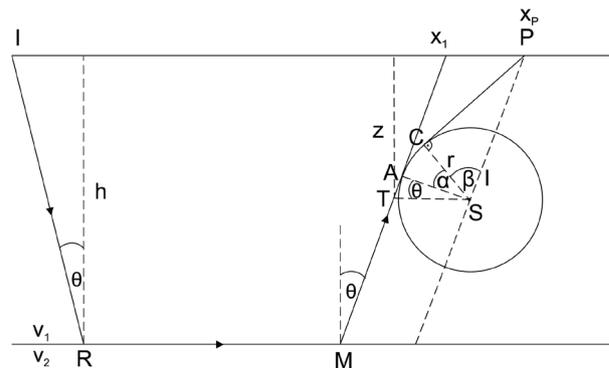

FIGURE 16
The ray from the source to the peak point through a series of line segments from the source I through the points R, M, T, A, C up to the peak point P.

The total traveltime is thus equal to the sum of the traveltimes in each segment:

$$t_\mathrm{p} = t_\mathrm{IR} + t_\mathrm{RM} + t_\mathrm{MT} + t_\mathrm{TA} + t_\mathrm{AC} + t_\mathrm{CP}, \qquad (A4)$$

equivalently:

$$t_p = \frac{s_{IR} + s_{MT} = s_{TA} + s_{AC} + s_{CP}}{v_1} + \frac{s_{RM}}{v_2}. \qquad (A4)$$

Figure A2 shows that:

$$s_{IR} = h/\cos\theta, s_{RM} = x_1 - 2h\tan\theta, s_{MT} = (h-z)/\cos\theta,$$
$$s_{TA} = r\tan\theta, s_{AC} = r\alpha, s_{CP}^2 = l^2 - r^2, \alpha = \pi/2 - \beta, \qquad (A5)$$
$$\cos\beta = r/l, l = z/\cos\theta, x_1 = x_p - r/\cos\theta, v_1/v_2 = \sin\theta,$$

which gives the final expression (7) for t_p.

REFERENCES

Alkhalifah T. and Fomel S. 2001. Implementing the fast marching eikonal solver: Spherical *versus* Cartesian coordinates. *Geophysical Prospecting* **49**, 165–178.

Baker J.A., Shoemaker M.L., Roark M., Anderson N. and Hinds R. 1997. *Reflection Seismic Mapping of Caverns and Collapsed Caves.* Carthage.

Buske S. and Kästner U. 2004. Efficient and accurate computation of seismic traveltimes and amplitudes. *Geophysical Prospecting* **52**, 313–322.

Cao S. and Greenhalgh S.A.1994. Finite-difference solution of the eikonal equation using an efficient first-arrival wavefront tracking scheme. *Geophysics* **59**, 632–643.

Ganji V., Gucunski N. and Maher A. 1997. Detection of underground obstacles by SASW method – numerical aspects. *Journal of Geotechnical and Geoenvironmental Engineering* **123**, 212–219.

Gelis C., Leparoux D., Virieux, J., Bitri A., Operto S. and Grandjean G. 2005. Numerical modeling of surface waves over shallow cavities. *Journal of Environmental and Engineering Geophysics* **10**, 111–121.

Gochioco L.M. 1990. Seismic surveys for coal exploration and mine planning. *The Leading Edge* **9**, 25–28.

Grandjean G. 2006. Imaging subsurface objects by seismic P-wave tomography: Numerical and experimental validations. *Near Surface Geophysics* **4**, 279–287.

Grandjean G. and Leparoux D. 2004. The potential of seismic methods for detecting cavities and buried objects: Experimentation at a test site. *Journal of Applied Geophysics* **56**, 93–106.

Grandjean G., Sénéchal G., Bitri A. and Daban J.B. 2002. Détection de carrières souterraines par sismique haute résolution à Annet-sur-Marne (France). *Comptes Rendus Geoscience* **334**, 441–447.

Herman G.C., Milligan P.A., Huggins R.J. and Rector J.W. 2000. Imaging shallow objects and heterogeneities with scattered surface waves. *Geophysics* **65**, 247–252.

Kim S. 2002. 3D eikonal solvers: First-arrival traveltimes. *Geophysics* **67**, 1225–1231.

Leidenfrost A., Ettrich N., Gajewski D. and Kosloff D. 1999. Comparison of six different methods for calculating traveltimes. *Geophysical Prospecting* **47**, 269–297.

Leparoux D., Bitri A. and Grandjean G. 2000. Underground cavities detection using seismic Rayleigh waves. *European Journal of Environmental and Engineering Geophysics* **5**, 33–53.

Mussett A.E. and Khan M.A. 2000. *Looking into the Earth: An Introduction to Geological Geophysics.* Cambridge University Press.

Park C.B., Miller R.D. and Xia J.1998. Ground roll as a tool to image a near-surface anomaly. 68th SEG meeting, New Orleans, Louisiana, USA, Expanded Abstracts, 874–877.

Piwakowski B., Tricot J.C., Leonard C., Ouarradi N. and Delannoy B.1997a. Underground tunnels detection and location by high-resolution seismic reflection. *Proceedings of 3rd Congress of European Section Environmental & Engineering Geophysical Society*, Aarhus, Denmark, 91–94.

Piwakowski B., Waletet, J. M. and Moreaux D. 1997b. High resolution seismic prospection of old gypsum mines – evaluation of detection possibilities. *European Journal of Environmental and Engineering Geophysics* **2**, 109–120.

Podvin P. and Lecomte I. 1991. Finite-difference computation of travel-times in very contrasted velocity models: A massively parallel approach and its associated tools. *Geophysical Journal International* **105**, 271–284.

Qin F., Luo Y., Olsen Q.B. and Schuster G.T. 1992. Finite-difference solution of the eikonal equation along expanding wavefronts. *Geophysics* **57**, 478–487.

Sun Y. and Fomel S. 1998. Fast marching eikonal solver in the tetragonal coordinates. *Stanford Exploration Project Report* **97**, 241–250.

Sethian J.A. 1996. *Level Set Methods.* Cambridge University Press.

Sethian J.A. and Popovici A.M. 1999. 3D traveltime computation using the fast marching method. *Geophysics* **64**, 516–523

Vanelle C. and Gajewski D. 2002. Second-order interpolation of travel-times. *Geophysical Prospecting* **50**, 73–83.

Vidale J.E. 1988. Finite-difference calculation of traveltimes. *Bulletin of the Seismological Society of America* **78**, 2062–2076.

Vidale J.E. 1990. Finite-difference calculation of traveltimes in three dimensions. *Geophysics* **55**, 521–526.